



Quench subcooled-jet impingement boiling: Staggered-array jets enhancement

Sang Gun Lee^a, Massoud Kaviany^b, Jungho Lee^{a,*}

^a Department of Energy Conversion Systems, Korea Institute of Machinery & Materials, Daejeon 34103, South Korea

^b Department of Mechanical Engineering, University of Michigan, Ann Arbor, MI 48109, USA

ARTICLE INFO

Article history:

Received 18 December 2018

Received in revised form 6 March 2019

Accepted 11 March 2019

Keywords:

Impinging jet

Staggered-array jet

Quench boiling heat transfer

Interacting jets

Cooling effectiveness

Inverse heat conduction

Subcooled boiling

ABSTRACT

In quench subcooled-jet boiling, an effective cooling of large surface area is achieved with jet arrays. Here a stainless-steel plate initially superheated at 900 °C is cooled with seven hexagonally arranged water [1 atm, 20 °C (80 °C subcooling)] jets (7j), and with varying jet separation distance (with a jet Reynolds number $Re_D = 5000$). Using high-definition visualization synchronized with the surface thermal characterization based on the inverse-conduction analysis allows calculation of the spatial and temporal variations of the local and average heat flux (q) and heat transfer coefficient (h). The local and temporal peaks in q and h occur under the jets with enhancements in the regions of their interactions. We compare these results with the prior two jets (2j) and single jet (1j) results (with $Re_D = 15,000$). For a jet separation of four nozzle diameter ($S/D_n = 4$), the 7j behavior is close to the single jet (1j), while with larger separation extra h peaks occur and the cooling becomes more effective (larger cooling area, but with smaller area-averaged heat transfer coefficient $\langle h \rangle$). For $S/D_n = 10$, the 7j enhanced cooling effectiveness is smaller than the 2j effectiveness, suggesting using similar total liquid flow rate, fewer jets are preferred. The cooling effectiveness enhancement for the $S/D_n = 6$ arrangement is the highest, reaching 50% and covering a large high- h area, and over a long elapsed time.

© 2019 Elsevier Ltd. All rights reserved.

1. Introduction

The system design challenge can avoid material instability in removal of very large heat flux by convection, while avoiding over-design and waste in rapid cooling of superheated surfaces. Impinging jet has been commonly used in material processing for its high heat and mass fluxes with the heat transfer coefficient exceeding 0.01 MW/m²-K under subcooled boiling [1,2]. The theoretical limits in heat flux and heat transfer coefficient h in boiling are discussed in [3,4] and for saturated water at 1 atm the theoretical maximum heat flux is 200 MW/m², and the h can reach 0.2 MW/m²-K using 3-D flow-boiling wicks. In steel production, rapid and uniform cooling of the material is necessary to ensure desirable mechanical and metallurgical properties, as reviewed by Wolf et al. [5]. To understand the mechanisms of impinging-jet cooling, theoretical [6], experimental [7] and numerical studies [8,9] have been conducted, including research on the single and multiple-jet impingement on stationary, superheated surfaces. Karwa et al. [10] provided visual observation of the dark zone underneath the single jet with surface temperature under 500 °C,

and showed that the peripheral boundary of this zone (called the wetting front) spreads radially with time. They suggested that the liquid deflection (ejection) occurs outside of wetting front due to surface tension and shear forces. Ishigai et al. [11] and Hall et al. [12] reported the coolant-surface contact at the stagnation point without any noticeable period of film boiling, even with an initial temperature >1000 °C. Hammad et al. [13] reported existence of a maximum heat flux in the nucleate boiling regime that changes into transition boiling within the fully-wetted region with the specific location varying with the surface wetting conditions. A more accurate location of the maximum heat flux was identified by Lee et al. [14]. Using high-resolution imaging, they analysed the hydrodynamics of the round water jet under very large initial superheat (900 °C) and large surface area. Synchronizing the boiling visualizations and the inverse conduction, they located the wetting front and evaluated the enhancement of heat transfer coefficient by the interaction of two adjacent jets and suggested an optimal jet-to-jet spacing [15]. The transient cooling effectiveness enhancement reached 65% compared to the single jet, at a spacing divided by nozzle diameter equal to 10.

The high heat and mass transfer fluxes and transfer coefficients of the impinging jet occurring in the stagnation region, cannot be advantageous in most cooling processes due to the

* Corresponding author.

E-mail address: jungho@kimm.re.kr (J. Lee).

Nomenclature

A	area, m^2
c_p	heat capacity, $J/kg\cdot K$
C	volumetric heat capacity, $J/m^3\cdot K$
D_n	nozzle diameter, m
h	heat transfer coefficient, $W/m^2\cdot K$
k	thermal conductivity, $W/m\cdot K$
Nu_D	Nusselt number based on nozzle diameter
q	heat flux, W/m^2
r	radial location, m
R_{do}	wetting-front radius, m
Re_D	Reynolds number based on nozzle diameter, m
s	unit step function
S	distance between jets in jet-array arrangement, m
t	time, s
T	temperature, $^{\circ}C$ or K
u	jet exit velocity, m/s
W	distance between jets for two-jet arrangement, m
Y	surface temperature variation
z	location from surface, m

Greek letters

λ	time step, s
μ	viscosity, $Pa\cdot s$
Δ	difference
ρ	density, kg/m^3
η	effectiveness

Subscripts and superscripts

c	estimated value
i	elapsed time
m	measured value
n	nozzle
∞	jet adiabatic temperature

Other

$\langle \rangle$	area average
-------------------	--------------

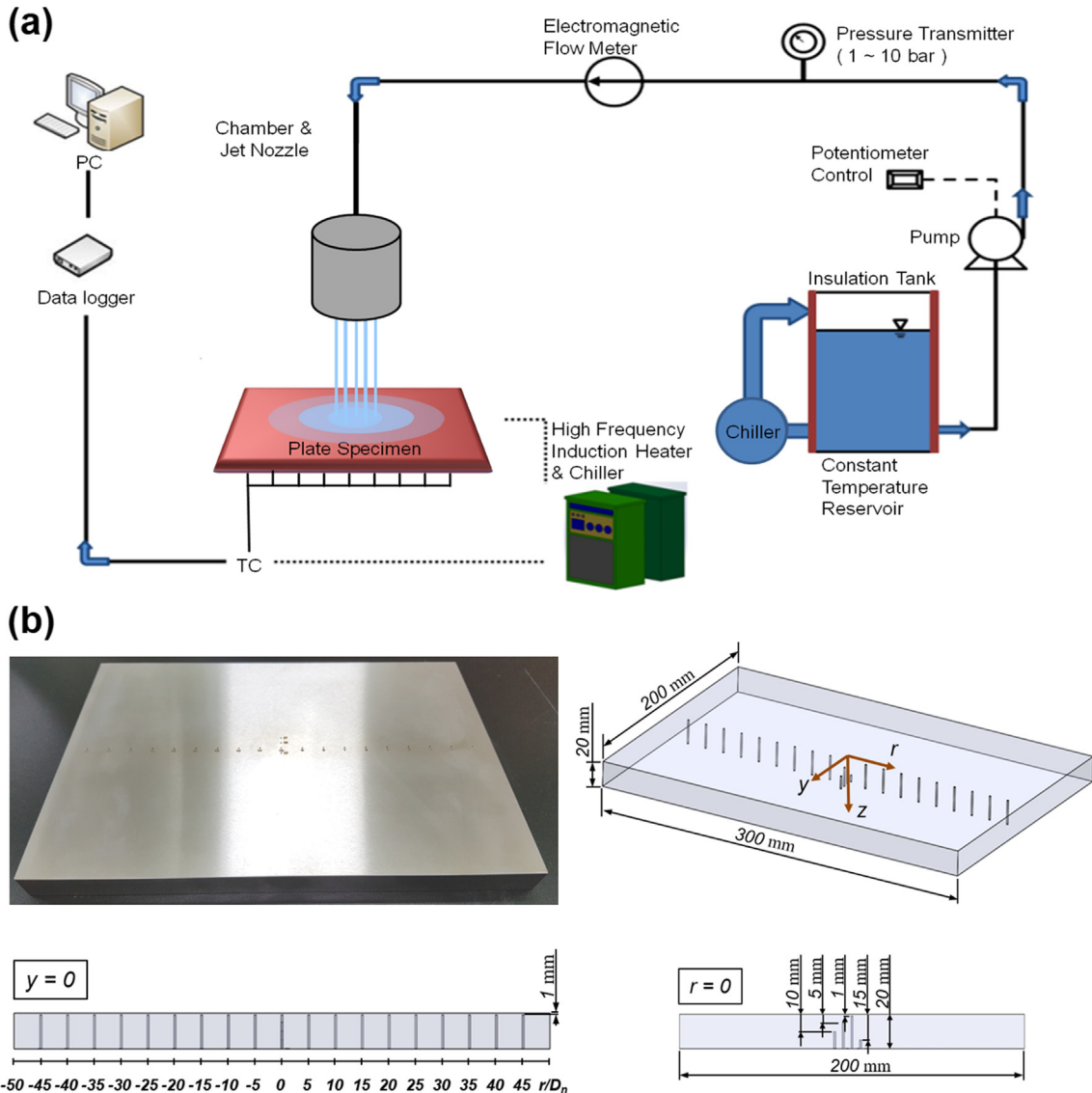


Fig. 1. Schematic of the (a) experimental setup of the staggered-array jet impingement cooling of a superheat stainless steel plate, and (b) the stainless steel flat plate with the location of the thermocouples.

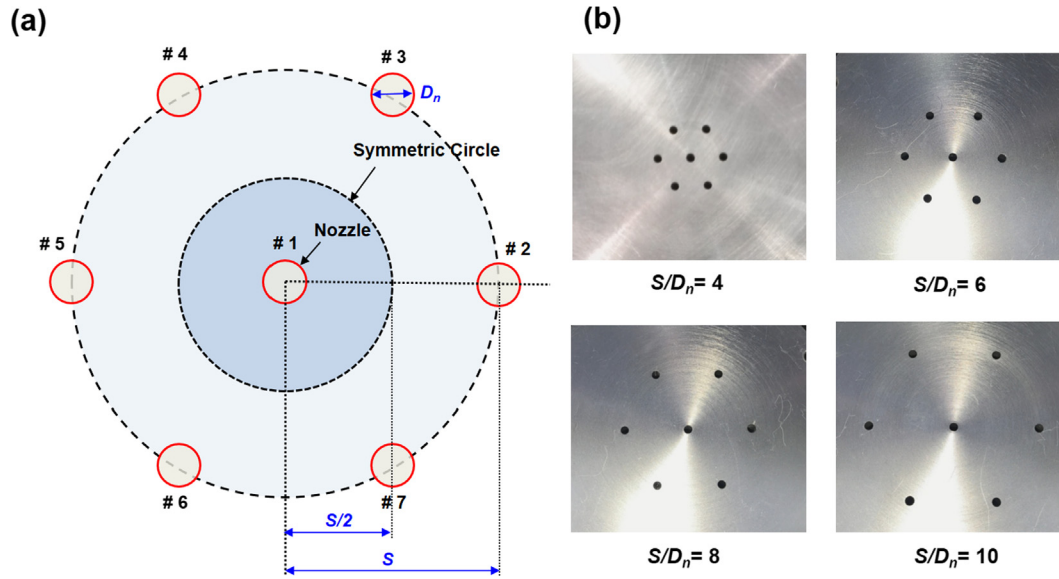


Fig. 2. (a) Geometry of the staggered-array jets, and (b) 4 staggered-array jets arrangements used in this study.

Table 1
Conditions for the current seven staggered-array jets and the previous single jet [14] and two interacting jets [15] subcooled quench boiling. The interjet distance W is used for the two-jet and S is used for the staggered-array jet arrangement.

N_j	D_n (mm)	Re_D	$\langle u \rangle_n$ (m/s)	$\langle u \rangle_n A_n$ (m ³ /s)	W/D_n , S/D_n
Single jet [14]	3	15,000	5.0	0.14	∞
Two jets [15]	3	15,000	5.0	0.28	10, 20, 30
Seven staggered-array jets [present]	3	5,000	1.7	0.327	4, 6, 8, 10

non-uniformity. While a small number of jets have effective local cooling, outside the inner regions the performance deteriorates owing to the low-momentum water supply. Also, the jet effectiveness has a limitation since there is no further cooling gain for Reynolds number $Re_D > 20,000$, due to severe flow deflection. So, designing an efficient distributed-jet system has attracted theoretical and practical interests [16–18], and it remains challenging the complexity of the jet interactions and various phase-change regimes occurring simultaneously in the cooling process [19,20]. So, understanding the impact of multiple-jet design parameters on the heat and mass transfer and their cooling performance are essential in search for effective cooling method with optimal threshold liquid flow. The staggered-array jets have potential for uniform cooling and the effect of the spatial arrangement of the jets on the flow and heat transfer have been reported [21,22]. Can et al. [23] investigated the heat transfer with a hexagonal array

of air jets and found a maximum area-averaged heat transfer coefficient at the spacing divided by the nozzle diameter $S/D_n = 5.5$, and independent of the nozzle to plate distance. At dimensionless pitches larger than 5.5, the impingement area per jet is large, resulting in lower area-averaged Nusselt number. For pitches smaller than 5.5, there is significant interaction between the jets reducing the radial jet velocity. Huber and Viskanta [24] used a square array of jets and their results are consistent with those of Can et al. [23] (maximum at $S/D_n = 6$). However, there has been no clear comparison between the results for the staggered-array jets and the single-jet.

Here, following our previous investigation of single-jet [14] and two interacting jets [15], we seek insight into the effect of the jet-to-jet spacing ($S/D_n = 4, 6, 8, 10$) of a staggered-array jets on the quench boiling phenomena and its hydrodynamics. While the literature provides many insights into the heat transfer performance of

Table 2
Uncertainty results for the estimated heat flux.

Uncertainty of influence coefficient	Measured temperature variation (ΔT^m)	± 5	$^{\circ}\text{C}$
	Thermal conductivity (k)	10.2	%
	Volumetric heat capacity (C)	4.8	%
Uncertainty of estimated heat flux	Heat flux range	0.5–5	MW/m ²
	Combined standard uncertainty	0.026–0.38	MW/m ²
	Total absolute uncertainty	0.052–0.76	MW/m ²
	Relative expanded uncertainty	10.3–15.2	%

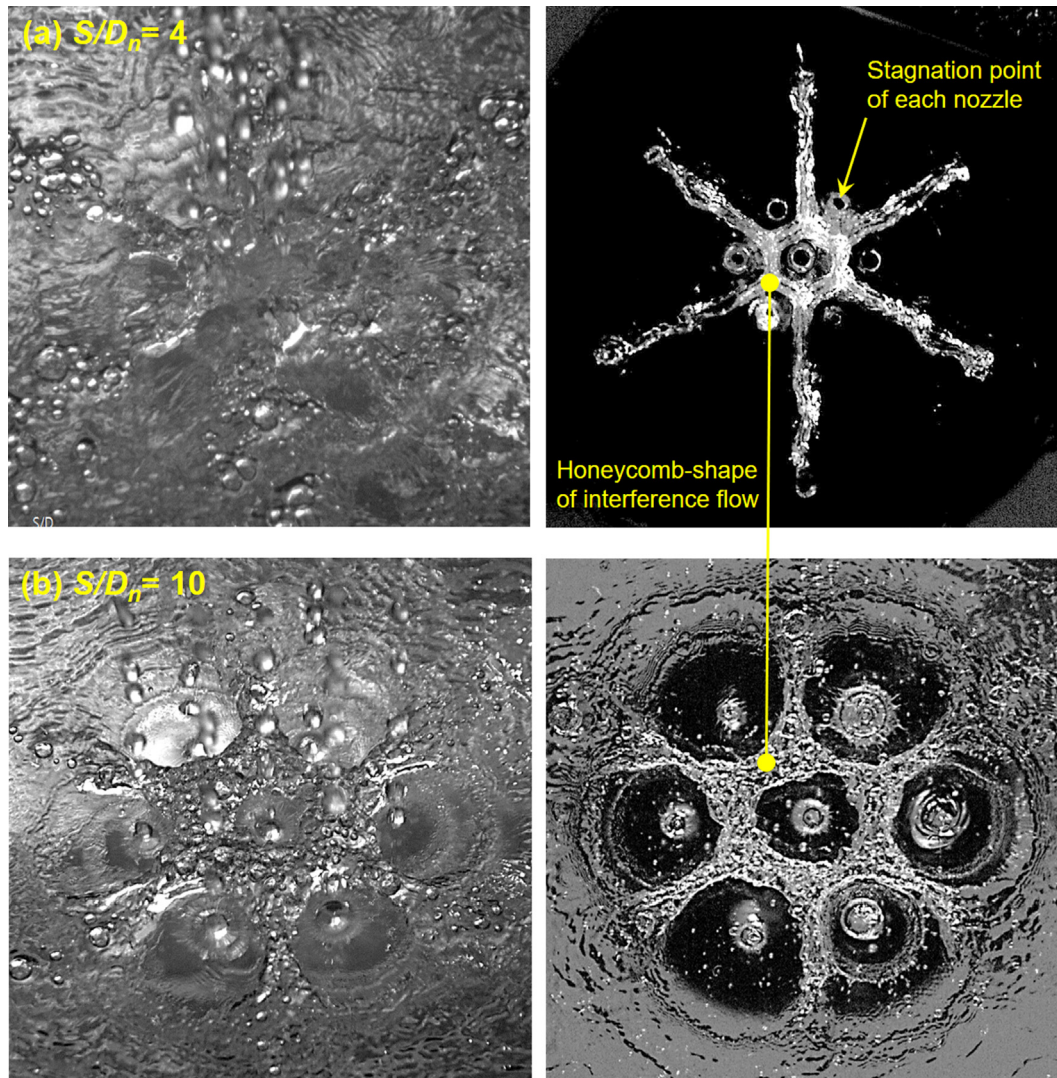


Fig. 3. Flow visualization of the staggered-array jets with the jet separation of (a) $S/D_n = 4$ and (b) $S/D_n = 10$.

the staggered-array jets, their interaction effectiveness have not been addressed. We use isothermal and boiling flow visualizations and the inverse heat conduction method to explore this heat transfer enhancement under similar conditions as the single jet and two jets studies, for a comprehensive comparison.

2. Experiment and methods

The experimental apparatus is schematically shown in Fig. 1(a) and is nearly identical to our previous work [14,15] for a comparison, and includes heat flux gauge, flow loop, data acquisition system (DAQ) and high-resolution camera. The flow loop consists of constant water temperature circulator, pump, electromagnetic flowmeter, water chamber, and nozzles. The jet water temperature is maintained at 20 ± 0.5 °C, with circulator in an insulated stainless-steel tank of 700 L, electric heater of 10 kW, and chiller. The cooling water is pumped (CRN 1-15, Grundfos) to the water chamber through the connecting flexible pipe and flow rate is measured by electromagnetic flowmeter (GF630A/LF600, Toshiba) with a measurement accuracy of $\pm 0.5\%$. The water flow rate for each jet is set at $0.327 \text{ m}^3/\text{h}$, corresponding to Reynolds number $Re_D = 5000$.

The measurement uncertainty is within 0.7%, for the volumetric flow rate measurement.

The heat flux gauge and thermocouple locations are shown in Fig. 1(b), and the stainless-steel ANSI 304 (8% Ni, 18% Cr, <0.08% C) rectangular plate has $300 \times 200 \times 20 \text{ mm}^3$ (length \times width \times thickness). This plate material is chemically inert and does not undergo solid-solid phase transformation which can affect the heat transfer and disturb the recorded temperature distribution during the quench process. To measure the temperature in real time, 22 holes ($1 \pm 0.1 \text{ mm}$ diameter) are drilled from the bottom surface with electric discharge machining (EDM). Nineteen of these have 19 mm depth (1 mm below the top surface), while radially 15 mm apart. The other three are at the plate center with depths of 5, 10 and 15 mm. The calibrated thermocouples (accuracy = ± 1 °C, KMTXL-0404G-6 OMEGA®) with diameter of 1 mm are inserted and held in place with spot welding. The temperature data is recorded by a data acquisition system (EX1032A, VTI Instruments Co.) at 10 data/s.

The staggered-array jets with a center nozzle ($D_n = 3 \text{ mm}$ inner diameter) and the hexagonally-placed six surrounding nozzles, are shown in Fig. 2(a). The nozzles in one row are laterally staggered

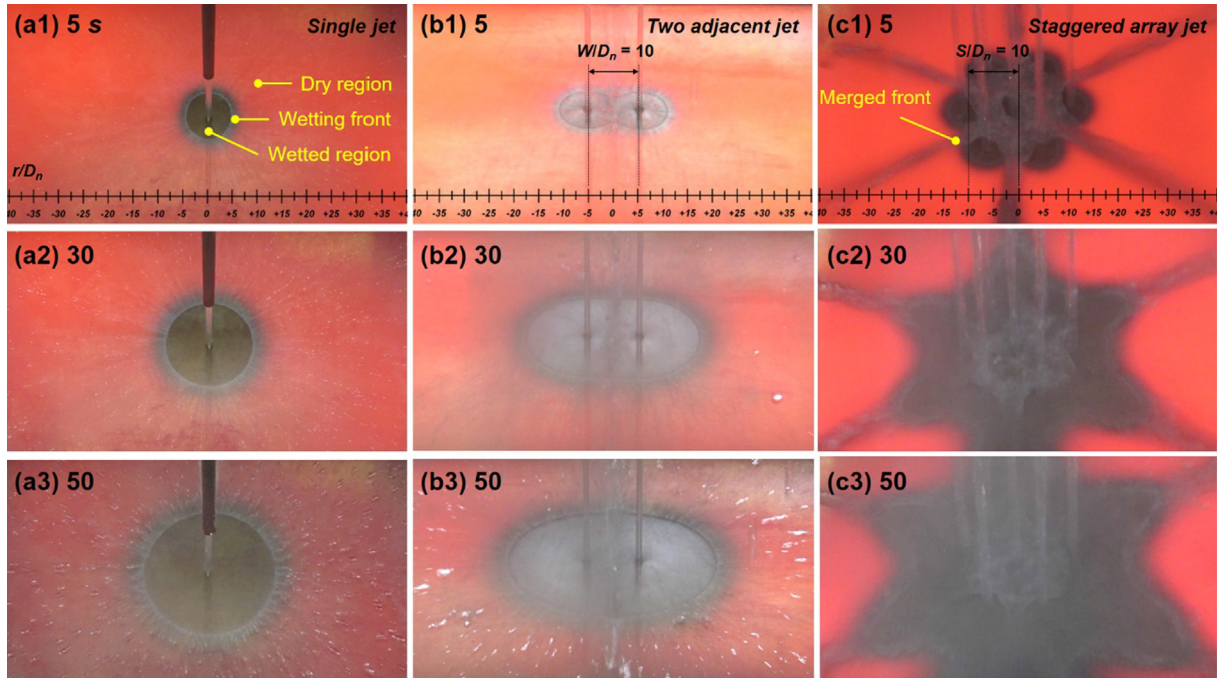


Fig. 4. Snapshot images of the single jet, the two jets ($W/D_n = 10$), and the staggered-array jets ($S/D_n = 10$) at three elapsed times of (a) 5, (b) 30, and (c) 50 s.

with respect to the nozzles in another row. They are clamped to the water chamber and mounted above the center of the heated plate with a separation distance of 100 mm. Bottom section of the water chamber was cut off to easily mount and demount the nozzle plates containing the jet array. The nozzles are made of stainless-steel tubing to ensure even flow distribution between the nozzles. The more detailed explanation is shown in Kim et al. [25] and Lee et al. [26]. Fig. 2(b) shows the image of various staggered-array jets with the distance ($S/D_n = 4, 6, 8, 10$) between the center nozzle and the surrounding nozzles. Table 1 summarizes the conditions for the experiments, as those in our previous studies for single and two-jet impingement quench boiling.

To quantify the boiling heat transfer characteristics, the surface temperature and heat flux are required and we solve the inverse heat conduction problem, described by Twomey [27] and Beck et al. [28], for their numerical estimations based on the recorded (thermocouples) plate internal temperature distribution. The local, instantaneous (at incremental elapsed time t_i) heat transfer coefficient $h(t_i)$ uses the surface temperature $T(0, r, t_i)$, surface heat flux (q), and the jet adiabatic temperature T_∞

$$h(t_i) = \frac{q^c(t_i)}{0.5[T^c(0, r, t_i) + T^c(0, r, t_{i-1})] - T_\infty} \quad (1)$$

where $T^c(0, r, t_i)$ and $q^c(t_i)$ are the estimated temperature and heat flux at time (t_i), and h is generally more accurate when evaluated at $t_{i-1/2}$.

The estimated heat flux at the surface is determined from the Fourier law by differentiating the calculated temperature using the Duhamel theorem [29,30] as

$$q^c(t_i) = -k \frac{\partial T^c}{\partial z} \Big|_{z=0} = -k \int_{t_0}^t \frac{\partial s(z, t - \lambda)}{\partial z} \Big|_{z=0} Y'(\lambda) d\lambda \quad (2)$$

where $Y(t_i)$ is the time-varying surface temperature, and λ is the time step. Here $s(z, t_i)$ is the unit step function which for a semi-infinite plate is

$$s(z, t_i) = 1 - \operatorname{erf}\left(\frac{z}{2\sqrt{\alpha t_i}}\right), \quad \frac{\partial s}{\partial z} \Big|_{z=0} = \frac{-1}{\sqrt{\pi \alpha t_i}} \quad (3)$$

The local Nusselt number is

$$Nu_D = \frac{hD_n}{k} \quad (4)$$

where D_n is the nozzle diameter and k is thermal conductivity of the water. This is averaged Nusselt number over the plate surface area as

$$\langle Nu_D \rangle = \frac{\langle h \rangle D_n}{k} = \frac{D_n}{k} \int_A h(t) \frac{[T(0, r, t) - T_\infty] dA}{\langle T(0, t) \rangle - T_\infty} \quad (5)$$

The uncertainty analysis is conducted for the numerically estimated heat flux. The uncertainty estimations include using mathematical models combining the individual uncertainties. Here we make this estimation with the following relations from ISO [31] and Beck et al. [32],

$$\begin{aligned} \delta q^c &= \sqrt{\sum_{i=1}^n \left(\frac{\partial q^c}{\partial x_i} \delta x_i \right)^2} \\ &= \sqrt{\left(\frac{\partial q^c}{\partial (\Delta T^m)} \delta \Delta T^m \right)^2 + \left(\frac{\partial q^c}{\partial k} \delta k \right)^2 + \left(\frac{\partial q^c}{\partial C} \delta C \right)^2} \end{aligned} \quad (6)$$

where ΔT^m , k and c_p are influence parameters for estimating the heat flux, and the uncertainties are presented in Table 2. The calculated results are summarized in Table 2, showing the uncertainties in the estimated heat flux uncertainty vary from 10.3 to 15.2% for the listed range of heat flux from 0.5 to 5 MW/m².

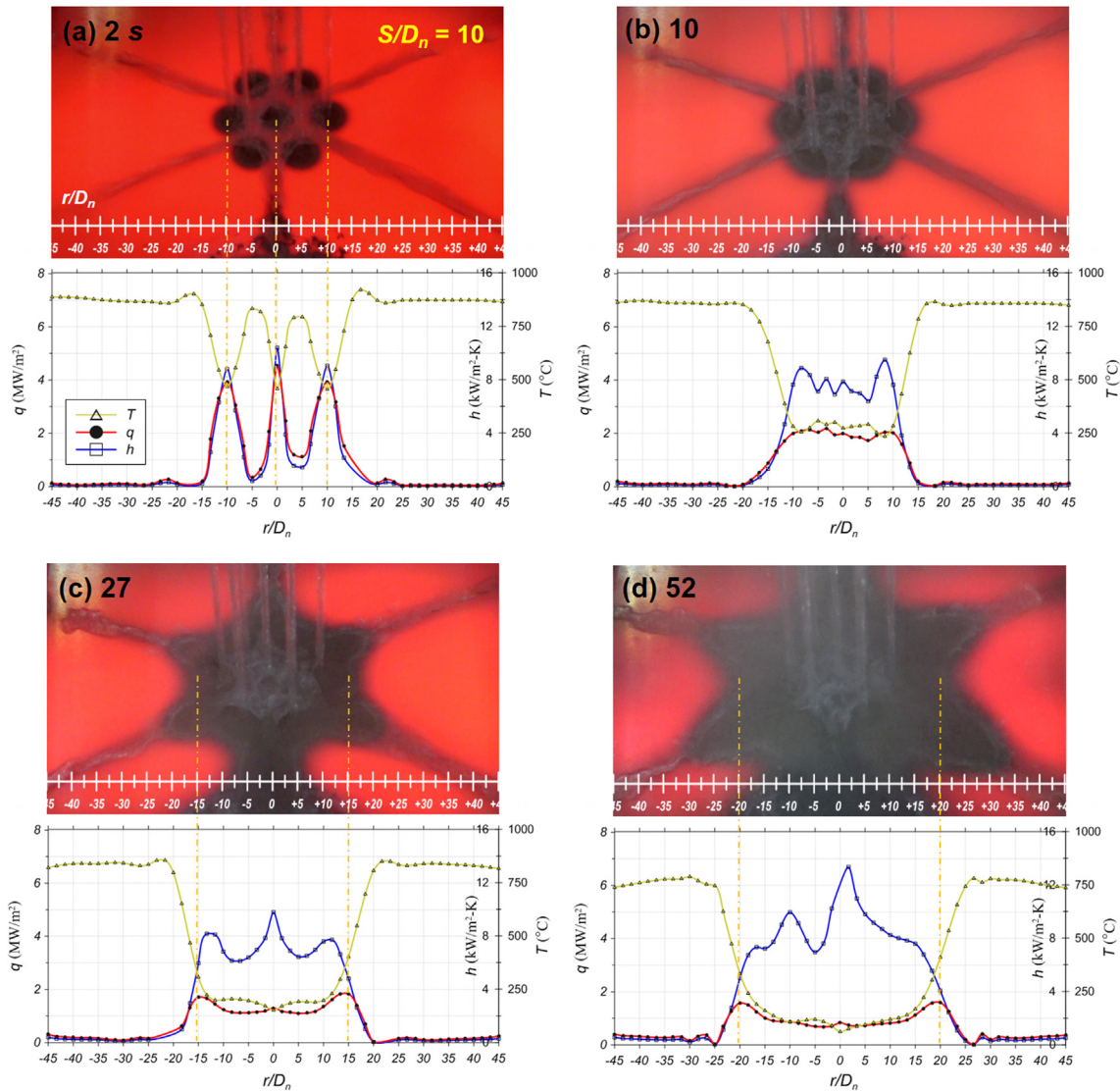


Fig. 5. Synchronization of boiling visualization of staggered-array jets ($S/D_n = 10$) with surface heat transfer characteristics (radial distributions of the temperature, heat flux and heat transfer coefficient) at elapsed time of (a) 2, (b) 10, (c) 27, and (d) 52 s.

3. Results and discussion

3.1. Visualization of staggered-array jets

Fig. 3 shows the snapshot of flow visualizations, without heat transfer (isothermal), with high-resolution video camera for two different S/D_n . The seven stagnation points (for each jet) are well represented with small circles and the jet flow interactions appear as each jet spreads radially and overlaps with others. This interacting flow occurs at the midpoint between each jet pairs and forms a honeycomb over a relatively small distance in Fig. 3(a) for $S/D_n = 4$. On the other hand, with large jet to jet spacing of Fig. 3(b) for $S/D_n = 10$, a larger honeycomb is formed of the interacting flows, covering a larger area. In the case of high Reynolds numbers ($Re_D > 10,000$), a large fraction of the coolants bounces off of the plate due to the high inertia of the individual jets opposing each other.

Fig. 4 is a comparison of boiling visualizations (snapshots) of the single jet, two jets ($W/D_n = 10$), and staggered-array jets ($S/D_n = 10$),

at three elapsed times. The three distinct regions, namely, merged front, wetting front, and dry are marked, and their characteristics are discussed in [14,26]. Fig. 4(b) and (c) are for two jets and staggered-array jets, respectively, with the same jet to jet distance ($W/D_n = S/D_n = 10$), and at the midpoint between the jets, the jets merge. In the staggered-array jets, complex and multiple merged flows are formed, where the center jet meets with six of the surrounding jets (the surrounding jets also meet each other). A time-varying boiling occurs and the wetting-front radius increases with the elapsed time, as shown in Fig. 4(c1), (c2) and (c3). The wetting-front follows the hexagonal contour due to diagonal flow emerging through the gap between the jets.

3.2. Boiling heat transfer of staggered-array jets

Fig. 5 is synchronized boiling visualizations combined with the radial distributions of the surface temperature, heat flux and the heat transfer coefficient for $S/D_n = 10$, at four elapsed times. In Fig. 5(a) with $t = 2$ s, the seven small wetting fronts (dark gray)

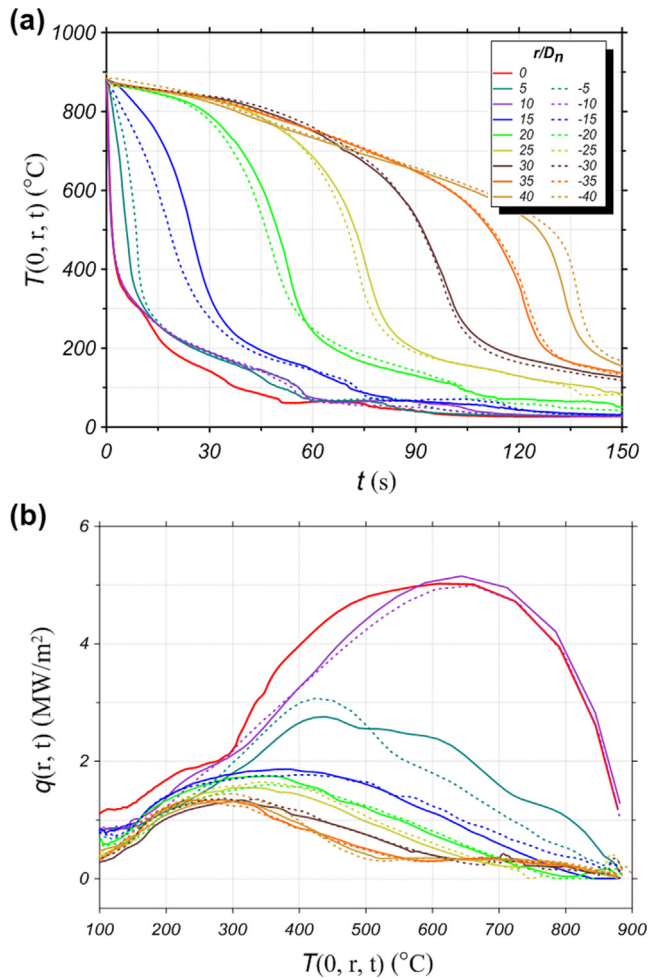


Fig. 6. Time history of the surface heat transfer characteristics (a) temperature variations with time, and (b) heat flux versus surface temperature, at various surface locations, for the staggered-array jets ($S/D_n = 10$).

are observed and each jet flow is rather isolated. The residual branches off the jets meet and form characteristic integrated, outward streams without wetting-fronts (due to the Leidenfrost effect at high surface temperatures). The red, blue and yellow line represent the heat flux, heat transfer coefficient and temperature, respectively. The peaks of the heat flux q are always consistent with the stagnation point of each jet (representing local rigorous cooling). So large temperature gradient is observed around the stagnation point. With increased elapsed time this sharp gradient is reduced and a uniform thermal behavior is observed over $r/D_n = -10$ to 10 , after 10 s, Fig. 5(b). The inner region consisting of jets reaches thermal equilibrium quicker than the outer region. This relates the spreading speed of the wetting front as described in [14]. The wetted region grows rapidly initially followed by a constant slower rate. As a result, a uniform temperature distribution is reached in the inner region. The outer region is marked with high heat flux and temperature gradient, due to nucleate boiling at the wetting front. This is shown in Fig. 5(c) and (d), until the entire surface is wetted, at elapsed time of 130 s. So, the position of the maximum heat flux moves from each jet stagnation point to the inner region, to the wetting front, and in the outer region, with increasing elapse time. In addition, the maximum heat flux is reduced with time, as the surface temperature drops.

Fig. 6 shows the time variations of the surface temperature and the heat flux versus the local surface superheat, at various radial locations. Around the jet stagnation points, $r/D_n = -10, 0$ and 10 , the largest gradients are observed in Fig. 6(a) and is accompanied by the highest heat flux of approximately 5 MW/m^2 . The next intense coolings are at $r/D_n = -5, +5$ located in the inner region, at which rigorous interactions between jets occur. The other effective coolings are at $r/D_n = -10, +10$ which are at the same distance as $r/D_n = -5, +5$ from jet stagnation points. However, it takes longer, approximately 15 s, until the temperature falls below 400°C . This highlights the cooling intensity contrast between the inner and outer regions.

Figs. 7 and 8 show the synchronization between boiling visualization and heat transfer characteristics of the $S/D_n = 4, 6, 8$ and 10 configurations and at elapsed time of 2 and 50 s. When the narrow jet strips ($S/D_n = 4$ and 6) develop, a relatively low temperature is observed in the inner region at 2 s, Fig. 7(a1) and (b1). A relatively uniform heat flux is established, as if there were similar flows over that area. After 50 s, Fig. 7(a2) and (b2), the wetted area (gray) for $S/D_n = 4$ occupies a smaller area compared to $S/D_n = 6$, because the momentum of radial jet flows is diminished from the rigorous interactions. Consequently, for both $S/D_n = 4$ and 6 similar uniform cooling in the inner region occurs, and for $S/D_n = 6$ is more advantageous. In Fig. 8(a1) and (b1), the temperature gradient is largest at the stagnation points, therefore, the uniform cooling performance is more pronounced for $S/D_n = 4, 6$. Comparing the wetted area at 50 s, Fig. 7(a2) for $S/D_n = 4$ has the smallest area and the other three in Fig. 7(b2), Fig. 8(a2) and (b2) show similar wetted area. So, the $S/D_n = 6$ results in the most desirable cooling performance (uniform cooling of the inner region and large spreading speed). In Fig. 7(b2), the heat flux shown in red has lower value within $-10 < r/D_n < 10$ compared with $-20 < r/D_n < 20$, where the nucleate boiling occurs. However, the surface temperature shown in yellow is much smaller compared the other regions, this results in the largest heat transfer coefficient. That shows that at the stagnation point, where the jet impinges, large the heat flux is maintained even when the temperature drops significantly. In particular, the case of $S/D_n = 6$ is rather optimal for maintaining high sensible heat flux (compared to $S/D_n = 4$ and 10) even though the surface temperature is lower.

3.3. Heat transfer enhancement by staggered-array jets

The distributions of the local (radial) heat transfer enhancement (h) of the staggered-array jets ($7j$) along the jet separation distance are compared with the single jet ($1j$) [14] (indicating infinite separation) and two jets ($2j$) [15] results. Fig. 9 shows these comparisons for ($W/D_n = 10$) and ($S/D_n = 10$) at elapsed times of $2, 5, 30$ and 50 s. The peaks of $1j, 2j$, and $7j$ at elapsed time of 2 s in Fig. 9(a) are consistent with the jet stagnation point performance ($1j, 2j$ and $7j$ have $1, 2$ and 3 of stagnation points, respectively). At 5 and 30 s in Fig. 9(b) and (c), these peaks move in the radial positions, marked by the nucleate boiling occurring at the wetting front.

Fig. 10 shows the distribution of the local heat transfer coefficient for the single jet and the staggered-array jets ($S/D_n = 4, 6$) at elapsed times of $2, 5, 30$, and 50 s. As mentioned above, the small jet separations of $S/D_n = 4$, and 6 show a uniform cooling in the inner region. So, comparing with Fig. 9(b), Fig. 10(b) does not show as many peaks. After 50 s, Fig. 10(d), several peaks in the outer region, and for the $7j$ has a considerably larger heat transfer coefficient within r/D_n from -10 to 10 . This is because the surface temperature is rather lower, but the heat flux remains high due to the forced convection heat transfer of the jets.

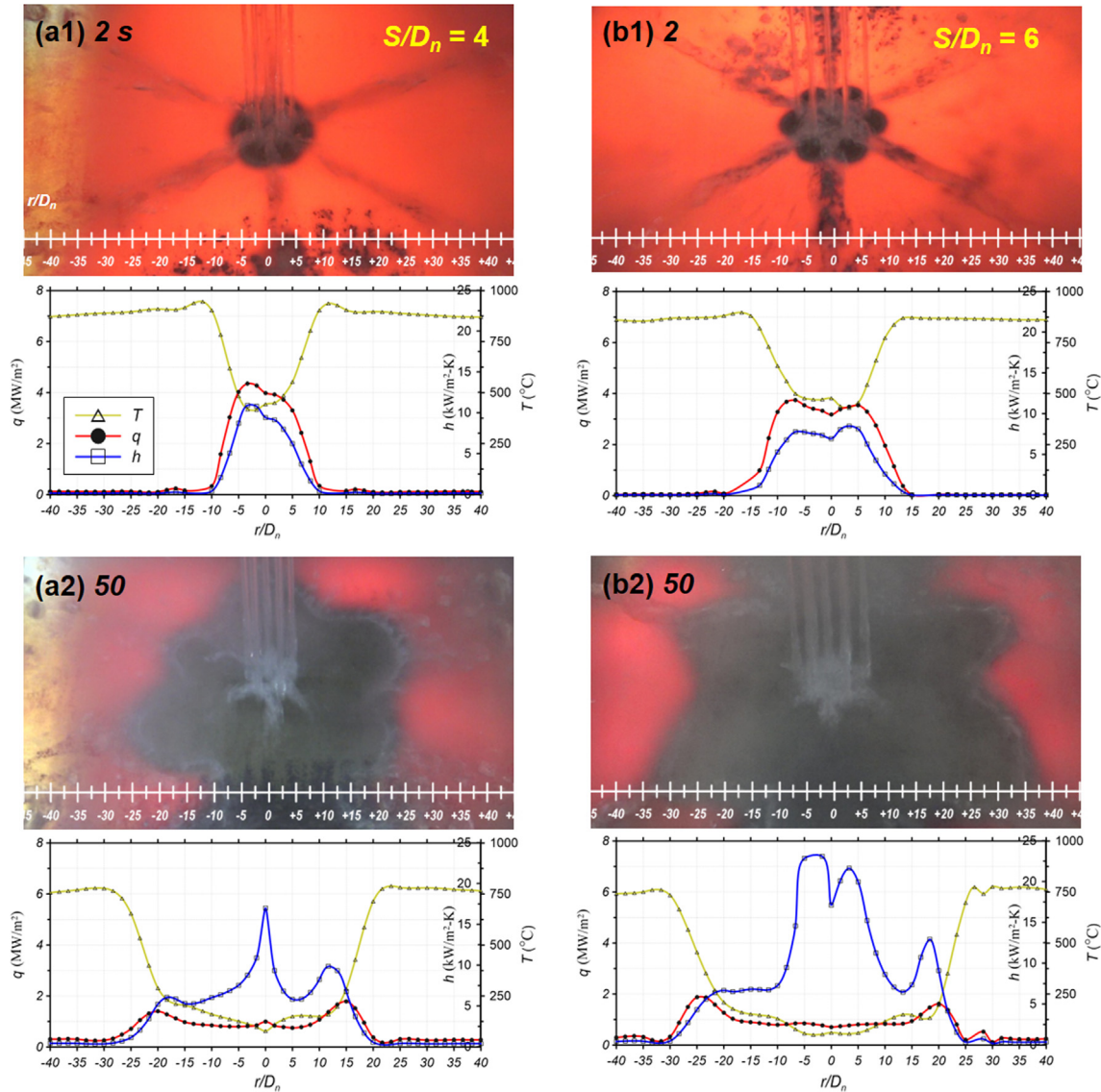


Fig. 7. Comparison of synchronization results of the temperature, heat flux and heat transfer coefficient of the staggered-array jets ($S/D_n = 4$ and 6) at elapsed time of 2 and 50 s.

Fig. 11 shows the time history of variations of enhancement effectiveness of the two jets ($W/D_n = 10$) and staggered-array jets ($S/D_n = 10$), which is calculated based on comparison with the single jet results. In order to quantify this enhancement for the optimal jet configuration, the effectiveness is defined for 2j and 7j, using the same total liquid flow rate accounting for the different Reynold numbers and the number of jets. These enhancement effectivenesses are (η_{2j} , η_{7j})

$$\eta_{2j} = \frac{A_{2j}}{2A_{1j}} \quad (7)$$

$$\eta_{7j} = \frac{A_{7j}}{7/3A_{1j}} \quad (8)$$

$$A_{1j, 7j} = \frac{1}{2} \int_{-R_{do}}^{R_{do}} h(r) 2\pi r dr \quad (9)$$

$$A_{2j} = \frac{1}{2} (1 - a) \int_{-R_{do}}^{R_{do}} h(r) 2\pi r dr \quad (10)$$

where A_{nj} is the area under the heat transfer coefficient curves of **Figs. 9 and 10**, for each jet configuration, and a is for area fraction in side circle of diameter $2R_{do}$ (presented in detail at [15]). So, the effectiveness of unity corresponds to the single jet.

In **Fig. 11**, the variations of the 2j and 7j effectiveness with respect to time show the maximum enhancement of 67% and 46% compared to that of a single jet, respectively. After these peak, both tend to attenuate over time. The effectiveness of the 2j and 7j fall below unity after 26 and 13 s, respectively, but after 45 s, the 7j returns toward unity again and remain there. So, the high Re_D of the 2j caused larger effectiveness peak, but the staggered-array jets enable maintaining a high effectiveness.

Fig. 12 shows the effectiveness enhancement (radial integration) for various jet separation of (a) two jets, and (b) staggered-

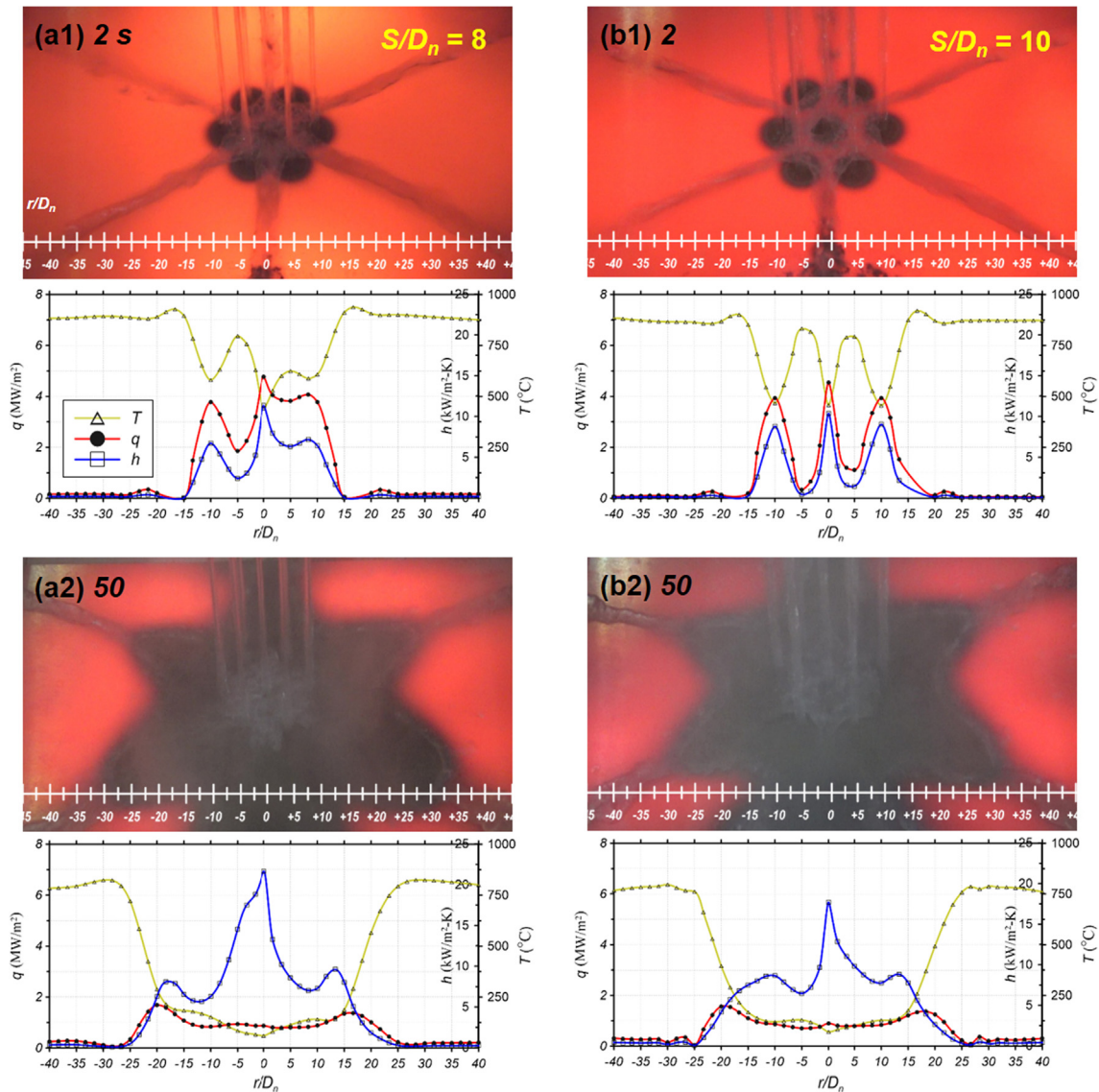


Fig. 8. Comparison of synchronization results of the temperature, heat flux and heat transfer coefficient of the staggered-array jets ($S/D_n = 8$ and 10) at elapsed time of 2 and 50 s.

array jets. In Fig. 12(a) for the 2j, the separation of $W/D_n = 10$ is the most effective, but lasts only 15 s. For the staggered-array jets of Fig. 12(b), the smaller separation peaks also appear at the beginning, but they lasts longer than the 2j. In particular, the effectiveness of the $S/D_n = 6$ remains high.

4. Conclusions

This staggered-array jets quench experimental study complements the quench (extreme surface superheat) boiling heat transfer of water jet impingement cooling previously reported for the single jet and two jets [14,15]. The additional parameter is the jet separation distance which creates distinct flow interactions around the inner jet region. The jet Reynolds number is adjusted considering the total mass flow rate for comparison and presentation of any heat transfer enhancement. The complex boiling regimes of the intensive cooling are characterized using synchro-

nized visualization (high-resolution video) and the numerical inverse heat conduction method.

The heat transfer characteristics in the inner and outer regions of the seven staggered-array jets were evaluated for various jet separation $S/D_n = 4, 6, 8$ and 10 . The difference in cooling effectiveness between the inner and outer regions is due to the intense emergence of the merging jet streams accompanied by a high heat transfer coefficient. The $S/D_n = 6$ configuration is the most effective combining a rather uniform and intense cooling in the inner region, with minimal adverse effect in the outer region. The enhancement of the staggered-array jets is compared with that of a single jet and two jets by defining and quantifying the jet interaction effectiveness and accounting for the total liquid flow rates. This cooling effectiveness enhancement for the $S/D_n = 6$ arrangement reaches 50% up to the elapsed time of 55 s. So, the proper separation distance for staggered-array jets results in (a) nearly uniform cooling, (b) high heat transfer coefficient, and (c) over a long elapsed time.

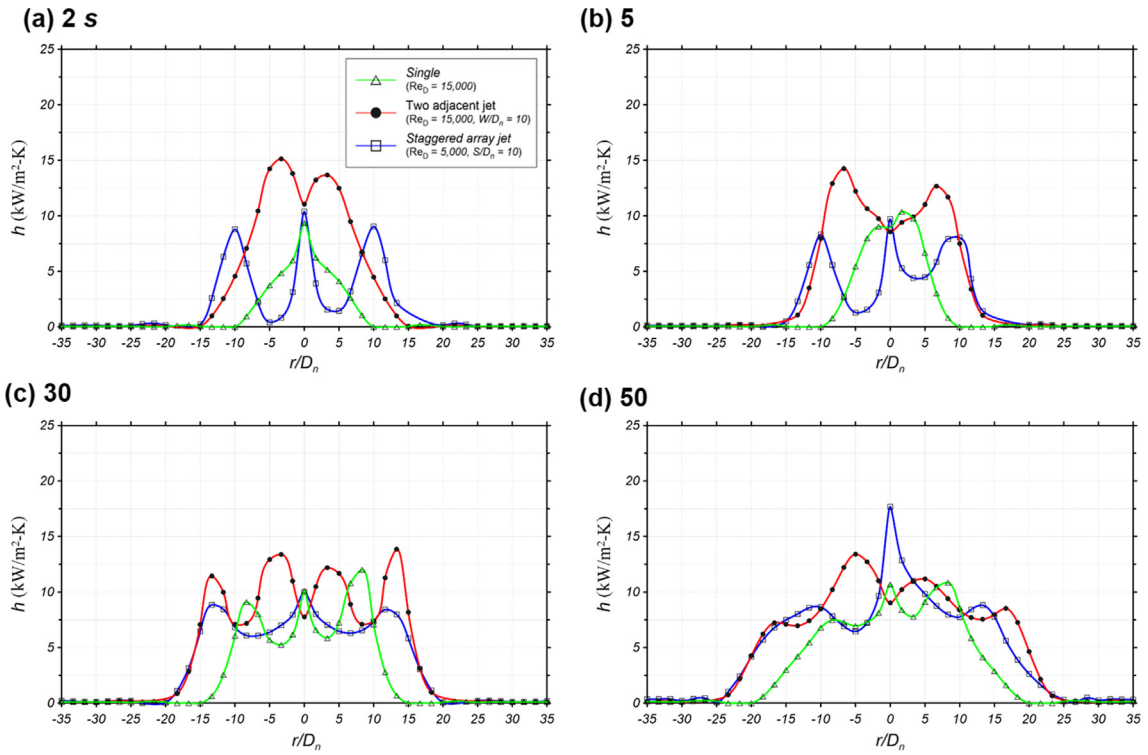


Fig. 9. Comparison of the radial heat transfer coefficient of the single jet (infinite separation), two jets ($W/D_n = 10$), and staggered-array jets ($S/D_n = 10$) at elapsed times of (a) 2, (b) 5, (c) 30, and (d) 50 s.

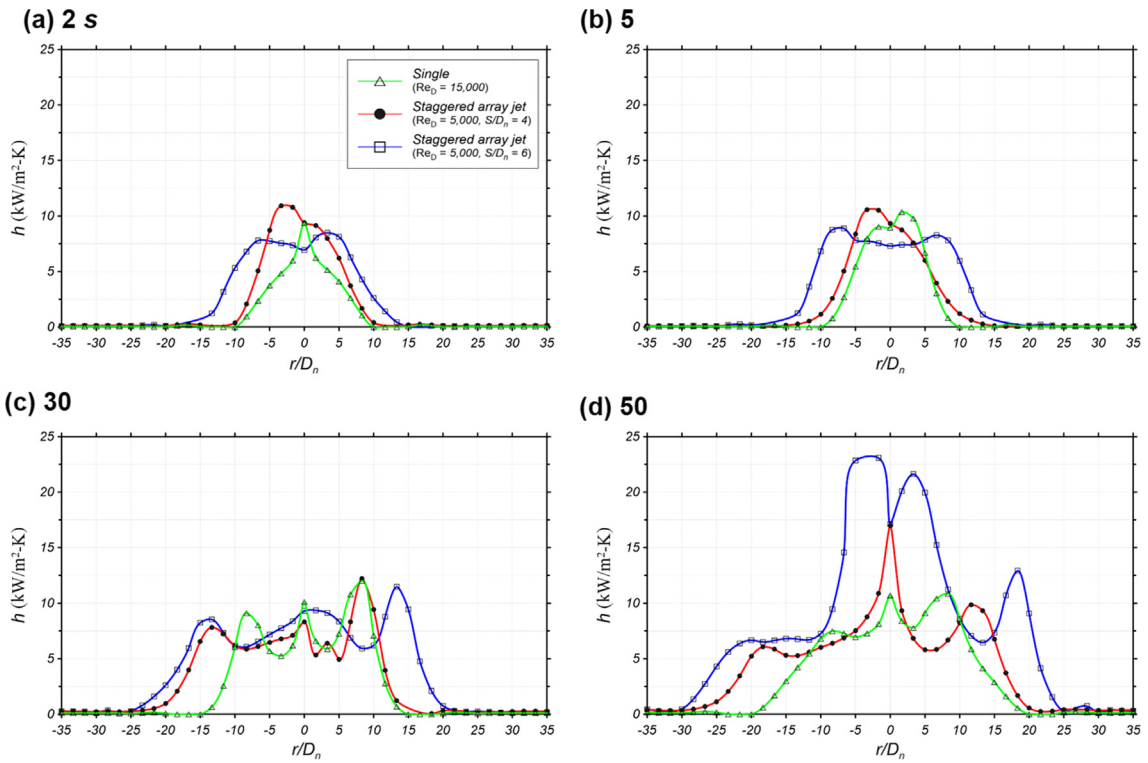


Fig. 10. Comparison of the radial heat transfer coefficient of the single jet and staggered-array jets ($S/D_n = 4, 6$) at elapsed times of (a) 2, (b) 5, (c) 30, and (d) 50 s.

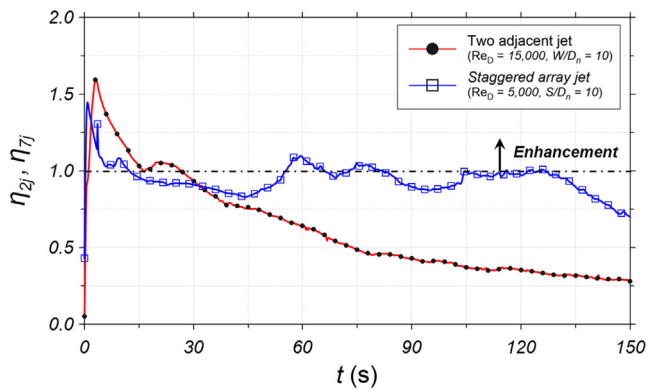


Fig. 11. Time variations of the effectiveness enhancement (radial integration) of the two jets ($W/D_n = 10$) and staggered-array jets ($S/D_n = 10$). Effectiveness of unity corresponds to performance of the single jet.

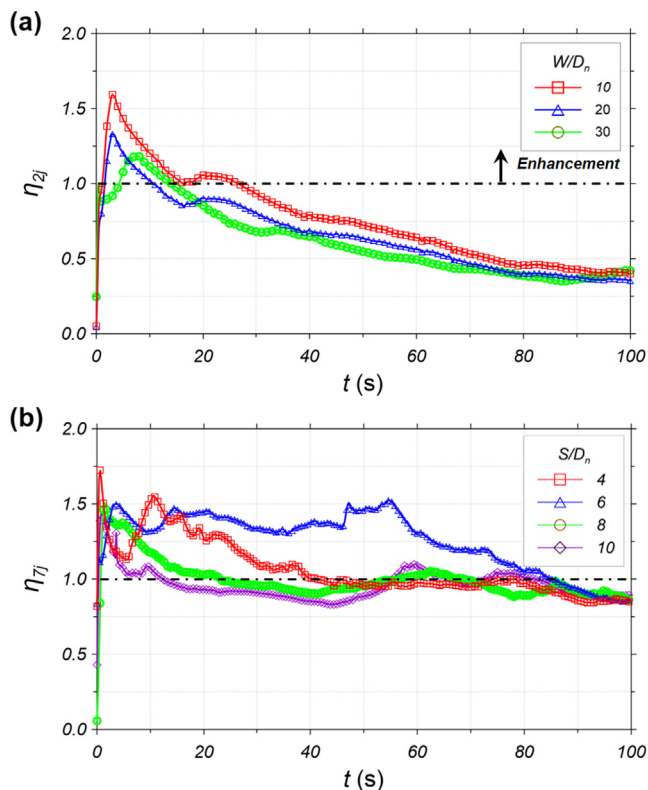


Fig. 12. Time variations of the effectiveness enhancement (radial integration) for various jet distance of (a) two adjacent jets, and (b) staggered-array jets.

Conflict of interest

The authors declared that there is no conflict of interest.

Acknowledgements

This work was supported by the National Research Council of Science and Technology (NST) grant funded by the Ministry of Science and ICT, South Korea (Grant No. KIMM-NK219B).

Appendix A. Supplementary material

Supplementary data to this article can be found online at <https://doi.org/10.1016/j.ijheatmasstransfer.2019.03.056>.

References

- [1] F.C. Kohring, Waterwall: water cooling systems, *Iron-Steel Eng.* 62 (1985) 30–36.
- [2] R. Viskanta, F.P. Incropera, Quenching with liquid jet impingement, *Heat Mass Transfer Mater. Process.* (1990) 455–476.
- [3] M. Kim, M. Kaviany, Flow-boiling canopy wick for extreme heat transfer, *Int. J. Heat Mass Transf.* 117 (2018) 1158–1168.
- [4] M. Kaviany, *Heat Transfer Physics*, second ed., Cambridge University Press, New York, 2014.
- [5] D.H. Wolf, F.P. Incropera, R. Viskanta, Jet impingement boiling, *Adv. Heat Transfer* 23 (1993) 1–132.
- [6] E.M. Sparrow, L. Lee, Analysis of flow field and impingement heat/mass transfer due to a nonuniform slot jet, *J. Heat Transfer* 97 (2) (1975) 191–197.
- [7] J. Lee, S.-J. Lee, The effect of nozzle configuration on stagnation region heat transfer enhancement of axisymmetric jet impingement, *Int. J. Heat Mass Transf.* 43 (10) (2000) 3497–3509.
- [8] H. Miyazaki, E. Silberman, Flow and heat transfer on a flat plate normal to a two-dimensional laminar jet issuing from a nozzle of finite height, *Int. J. Heat Mass Transf.* 15 (1972) 2097–2107.
- [9] E.J. Watson, The radial spread of a liquid jet over a horizontal plate, *J. Fluid Mech.* 20 (3) (1964) 481–489.
- [10] N. Karwa, T. Gambaryan-Roisman, P. Stephan, C. Tropea, Experimental investigation of circular free-surface jet impingement quenching: Transient hydrodynamics and heat transfer, *Exp. Therm. Fluid Sci.* 35 (2011) 1435–1443.
- [11] S. Ishigai, S. Nakanishi, T. Ochi, Boiling heat transfer for plane water jet impinging on a hot surface, in: *Proceedings of the Sixth International Heat Transfer Conference*, Toronto, Ont., Canada, August 1978.
- [12] D.E. Hall, F.P. Incropera, R. Viskanta, Jet impingement boiling from a circular free-surface jet during quenching: part 1—single-phase jet, *J. Heat Transfer* 123 (2001) 901–910.
- [13] J. Hammad, Y. Mitsutake, M. Monde, Movement of maximum heat flux and wetting front during quenching of hot cylindrical block, *Int. J. Therm. Sci.* 43 (2004) 743–752.
- [14] S.G. Lee, M. Kaviany, C.J. Kim, J. Lee, Quasi-steady front in quench subcooled-jet impingement boiling: Experiment and analysis, *Int. J. Heat Mass Transf.* 113 (2017) 622–634.
- [15] S.G. Lee, M. Kaviany, J. Lee, Quench subcooled-jet impingement boiling: Two interacting-jet enhancement, *Int. J. Heat Mass Transf.* 126 (2018) 1302–1314.
- [16] G.H. Jirka, P.J. Akar, Hydrodynamic classification of submerged multiport-diffuser discharges, *J. Hydraulic Eng.* 117 (9) (1991) 1113–1128.
- [17] J.H. Lee, G.H. Jirka, Multiport diffuser as line source of momentum in shallow water, *Water Resour. Res.* 16 (4) (1980) 695–708.
- [18] H.J. Wang, M.J. Davidson, Jet interaction in a still ambient fluid, *J. Hydraulic Eng.* 129 (5) (2003) 349–357.
- [19] B.S. Pani, J.H. Lee, A.C. Lai, Application of Reichardt's hypothesis for multiple coflowing jets, *J. Hydro-Environ. Res.* 3 (3) (2009) 121–128.
- [20] K.L. Pun, M.J. Davidson, H.J. Wang, Merging jets in a coflowing ambient fluid—a hybrid approach, *J. Hydraulic Res.* 38 (2) (2000) 105–114.
- [21] L.F.G. Geers, Multiple Impinging Jet Arrays: An Experimental Study on Flow Hand Heat Transfer Ph.D Thesis, Delft University of Technology, 2004.
- [22] B. Weigand, S. Spring, Multiple jet impingement a review, *Heat Transfer Res.* 42 (2) (2011).
- [23] M. Can, A.B. Etemoğlu, A. Avcı, Experimental study of convective heat transfer under arrays of impinging air jets from slots and circular holes, *Heat Mass Transf.* 38 (2002) 251–259.
- [24] A.M. Huber, R. Viskanta, Effect of jet-jet spacing on convective heat transfer to confined, impinging arrays of axisymmetric air jets, *Int. J. Heat Mass Transf.* 37 (18) (1994) 2859–2869.
- [25] T. Kim, D.W. Oh, K.H. Do, J.M. Park, J. Lee, Effect of initial temperature of a cylindrical steel block on heat transfer characteristics of staggered array jets during water jet quenching, *Heat Transfer Eng.* 36 (12) (2015) 1037–1045.
- [26] S.G. Lee, J.S. Kim, D.H. Shin, J. Lee, Boiling heat transfer characteristics of staggered-array water impinging jets on hot steel plate, *J. Heat Transfer* 140 (3) (2018) 030903.
- [27] S. Twomey, The application of numerical filtering for the solution of integral equations encountered in indirect sensing measurements, *J. Franklin Instit.* 279 (1965) 95–109.
- [28] J.V. Beak, B. Blackwell, C.R. St. Clair, *Inverse Heat Conduction*, Wiley, New York, 1985.
- [29] J.V. Beak, Transient sensitivity coefficient for the thermal contact conductance, *Int. J. Heat Mass Transf.* 10 (1967) 1615–1616.
- [30] J.V. Beak, Determination of optimum, transient experiments for thermal contact conductance, *Int. J. Heat Mass Transf.* 12 (1969) 621–633.
- [31] ISO, Guide to the Expression of Uncertainty in Measurement, International Organization for Standardization, Geneva, 1995.
- [32] B. Blackwell, J.V. Beak, A technique for uncertainty analysis for inverse heat conduction problems, *Int. J. Heat Mass Transf.* 53 (2010) 753–759.